

On the sound produced by a flapping flag

A. Manela

Department of Mathematics, Massachusetts Institute of Technology, Cambridge, MA 02139, USA

M.S. Howe

Boston University, College of Engineering, 110 Cummington Street, Boston MA 02215, USA

A linear theory is proposed for the motion and sound production of a flag in nominally uniform high Reynolds number flow. The flag is modelled as an elastic fluid-loaded filament subject to either clamped-free or fixed-free boundary conditions. Eigenfunctions describing standing waves in the absence of fluid loading are used to expand the loaded flag deflection. The resulting temporal stability problem is analysed and the neutral curve and modes of motion describing the transition to instability are discussed in detail for each boundary condition. It is found that the fixed-free flag is considerably more stable than the clamped-free flag. In the limit of a very heavy flag, instability sets in as a resonant standing wave, while lighter flags exhibit flutter (convective) instability. Acoustic radiation of dipole type is calculated and discussed in the limit where the flag is acoustically compact. At the onset of instability it is found that the acoustic pressure is dominated by the contribution of the wake term and that light flags are noisier than heavy.

I. Introduction

The fundamental fluid-structure interactions involved in the motion of a flag is of continuing and intense interest.¹ It is probably the simplest of a whole range of related mechanical problems that include, for example, the fluttering associated with both snoring² and the instabilities encountered in industrial printing machines.³ Similar flapping motions are known to improve the efficiency of propulsive swimming,⁴ and are believed to reduce turbulent drag during locomotion.⁵

Taneda⁶ has investigated the motion of a flag experimentally in a wind tunnel. Zhang *et al.*⁷ and Zhu and Peskin⁸ have examined an analogue problem involving flexible filaments in flowing soap films. Watanabe *et al.*^{3,9} examined the fluttering motion of paper both experimentally and numerically, using a time-marching scheme applied to the full Navier-Stokes equations and a low-order eigenfunction expansion assuming the flow is potential. More recently Shelley *et al.*¹⁰ experimented with a flag in a water tunnel and compared their observations with predictions of ‘heavy-flag’ theory. A linearised treatment for the problem has been suggested by Argentina and Mahadevan,¹¹ where a simplified mathematical description of the fluid loading effect was assumed based on classical thin airfoil theory.¹² Connell and Yue¹³ have devised a non-linear, numerical scheme that couples the flag motion to an incompressible wind governed by the Navier-Stokes equations. Alben and Shelley¹⁴ have also considered the non-linear dynamics of the flag, predicting phenomena such as bistability and transition to chaos.

Most of these studies model the flag as a thin elastic membrane. The flag equation of motion then involves a balance between flag inertia, fluid loading, and a fourth order derivative of the flag displacement representing the stiffness response. The validity of such a formulation for a cloth flag is questionable, because a non-dimensional representation of the stiffness contribution reveals it to be small over its whole length (except possibly in the immediate neighbourhood of the free end). Yet, as some of the above studies indicate (see, e.g.,¹³), it appears to be necessary to retain stiffness in the equation of motion to ensure robustness of the structural numerical model. Physically, it is not the introduction of this term into the equation that matters but the consequent requirement to impose four boundary conditions. The effect of these conditions on the resulting motion is crucial. All of the aforementioned studies consider the case of a clamped-free flag, where a vanishing deflection and angle of deflection are assumed at the pole. However, casual observation indicates that the latter may not be appropriate in practice. A goal of the present contribution is therefore

to examine the effect of replacing the clamped-free condition by the more appropriate condition that the bending moment should vanish. This is in addition to the other objective of calculating the sound produced by the motion of the flag.

We consider the linearized problem and make use of the simplified fluid loading model suggested by Theodorsen¹² and applied by Argentina and Mahadevan.¹¹ The mathematical problem is formulated in Sec. II. The corresponding eigenvalue problem for the self-excited motion and its outcome, the critical conditions for transition to flapping motion, are discussed in Sec. III. In Sec. IV the acoustic radiation is calculated for a compact flag. Some concluding remarks are made in Sec. V.

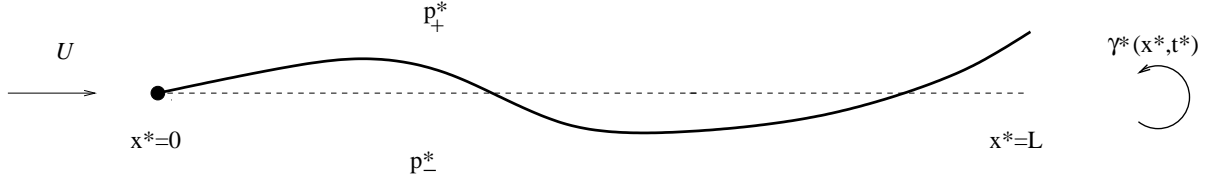


Figure 1. Setup of the problem. The flag pole is located at $x^* = 0$ and its free end is at $x^* = L$. The inertial fluid loading is $\Delta p^* = p_-^* - p_+^*$ and the circulation per unit length of the shedded vortex sheet is $\gamma^*(x^*, t^*)$.

II. The governing equations

Consider nominally uniform flow of air of mean density ρ_0 at speed U over an inextensible flag of streamwise length L and mass ρ_s per unit area (Figure 1). In the undisturbed state the flag occupies the interval $0 < x^* < L$ of the x^* axis, has thickness h and span l , where $h \ll L \ll l$, and is connected to a flag pole at $x^* = 0$, where x^* is measured in the direction of the mean flow. The motion is assumed to be two-dimensional, uniform with respect to spanwise position parallel to the flag pole, and of high Reynolds number $UL/\nu \gg 1$, where ν is the kinematic viscosity of the air. For simplicity, we neglect the effect of frictional drag. Small amplitude deflections $\xi^*(x^*, t^*)$ of the flag from an undisturbed planar form (in the direction of the y^* -axis normal to the undisturbed plane of the flag) are taken to be governed in the linearized approximation by

$$\rho_s \frac{\partial^2 \xi^*}{\partial t^{*2}} + EI \frac{\partial^4 \xi^*}{\partial x^{*4}} - \Delta p^* = 0, \quad (1)$$

where EI is the bending stiffness of the flag (E being Young's modulus and $I = h^3/12$ the moment of inertia coefficient per unit span) and $\Delta p^* = p_-^* - p_+^*$ is the inertial pressure loading (representing the 'added mass') in the direction of positive ξ^* (Figure 1). A dimensionless representation of the problem is achieved by normalizing distances by the flag length L and pressure by $\rho_0 U^2$. To obtain a dimensionless balance between inertial and elastic effects we scale the time by L/U_b , where $U_b = \sqrt{EI/\rho_s L^2}$ is the characteristic bending wave velocity. Substituting these into (1) and denoting non-dimensional variables by the omission of asterisks, we have

$$\frac{\partial^2 \xi}{\partial t^2} + \frac{\partial^4 \xi}{\partial x^4} - \frac{\alpha^2}{\mu} \Delta p = 0 \quad (2)$$

where $\mu = \rho_s/\rho_0 L$ is the non-dimensional flag mass and $\alpha = U/U_b$ the normalized wind speed.

The inertial pressure jump Δp is predominantly attributable to the effect of added mass, and is determined as a superposition of non-circulatory (nc) and circulatory (c) flows associated respectively with the potential flow motion of the relatively large scale flow induced by the motion of the flag and vortex shedding from the flag trailing edge. Assuming a slowly varying transverse velocity of the fluid along the filament, we make use of the approximate airfoil theory of Theodorsen¹² and write for the non-circulatory velocity potential (scaled by LU) along the flag

$$\phi_{nc} = \pm \sqrt{x(1-x)} \left(\frac{1}{\alpha} \frac{\partial \xi}{\partial t} + \frac{\partial \xi}{\partial x} \right). \quad (3)$$

The positive and negative signs correspond respectively to the 'upper' and 'lower' surfaces ($y = \pm 0$) of the flag. Applying Bernoulli equation and neglecting terms $O(\partial^2 \xi / \partial x^2, \partial^2 \xi / \partial x \partial t)$ for consistency with the

above approximation, we obtain for the non-circulatory pressure jump

$$\Delta p_{nc} = \frac{2x-1}{\sqrt{x(1-x)}} \left(\frac{1}{\alpha} \frac{\partial \xi}{\partial t} + \frac{\partial \xi}{\partial x} \right) - \frac{2}{\alpha^2} \sqrt{x(1-x)} \frac{\partial^2 \xi}{\partial t^2} \quad (4)$$

which preserves the square-root leading- and trailing-edge singularities together with the added-mass term. The significance of this approximation is discussed further in Sec. V.

To obtain a finite velocity at the trailing edge, the circulatory flow associated with vortex shedding from the free end must be considered. Let $\gamma = \gamma(x_v, t)$ (with $1 < x_v < \infty$, see Fig. 1) denote the circulation per unit length of the vortex sheet wake. The circulatory velocity potential is then¹²

$$\phi_c = -\frac{1}{4\pi} \int_1^\infty \arctan \left(\frac{\sqrt{x(1-x)(x_v^2-1)}}{(1+x_v)/2 - xx_v} \right) \gamma(x_v, t) dx_v. \quad (5)$$

The circulation $\gamma(x_v, t)$ is determined by the Kutta condition, requiring that no infinite velocities occur at the trailing edge. Therefore,

$$\left(\frac{\partial \phi_{nc}}{\partial x} + \frac{\partial \phi_c}{\partial x} \right)_{x=1} \text{ must be finite.}$$

Substitution of (3) and (5) into the above yields the condition

$$\frac{1}{2\pi} \int_1^\infty \sqrt{\frac{x_v+1}{x_v-1}} \gamma(x_v, t) dx_v = \left(\frac{1}{\alpha} \frac{\partial \xi}{\partial t} + \frac{\partial \xi}{\partial x} \right)_{x=1}. \quad (6)$$

The circulatory pressure jump associated with ϕ_c in (5) is

$$\Delta p_c = -\frac{1}{2\pi \sqrt{x(1-x)}} \int_1^\infty \frac{2x+x_v-1}{\sqrt{x_v^2-1}} \gamma(x_v, t) dx_v. \quad (7)$$

Making use of relation (6), we obtain

$$\Delta p_c = -\frac{2C(\gamma) - 1 + 2x(1 - C(\gamma))}{\sqrt{x(1-x)}} \left(\frac{1}{\alpha} \frac{\partial \xi}{\partial t} + \frac{\partial \xi}{\partial x} \right) \quad (8)$$

where $C(\gamma)$ is the Theodorsen function¹²

$$C(\gamma) = \frac{\int_1^\infty \frac{x_v}{\sqrt{x_v^2-1}} \gamma(x_v, t) dx_v}{\int_1^\infty \sqrt{\frac{x_v+1}{x_v-1}} \gamma(x_v, t) dx_v}. \quad (9)$$

The total pressure jump is therefore given by

$$\Delta p = \Delta p_{nc} + \Delta p_c = -2C(\gamma) \sqrt{\frac{1-x}{x}} \left(\frac{1}{\alpha} \frac{\partial \xi}{\partial t} + \frac{\partial \xi}{\partial x} \right) - \frac{2}{\alpha^2} \sqrt{x(1-x)} \frac{\partial^2 \xi}{\partial t^2}. \quad (10)$$

We examine solutions of equation (2) that satisfy either ‘fixed-free’

$$\xi(0, t) = 0, \quad \frac{\partial^2 \xi}{\partial x^2}(0, t) = 0, \quad \frac{\partial^2 \xi}{\partial x^2}(1, t) = 0, \quad \frac{\partial^3 \xi}{\partial x^3}(1, t) = 0 \quad (11)$$

or ‘clamped-free’

$$\xi(0, t) = 0, \quad \frac{\partial \xi}{\partial x}(0, t) = 0, \quad \frac{\partial^2 \xi}{\partial x^2}(1, t) = 0, \quad \frac{\partial^3 \xi}{\partial x^3}(1, t) = 0 \quad (12)$$

boundary conditions.

III. Temporal stability analysis

A. The eigenvalue problem

Assuming exponential time dependence

$$\xi(x, t) = \zeta(x) \exp[-i\omega t], \quad (1)$$

we obtain respectively from (2) and (10)

$$-\omega^2 \zeta + \zeta'''' - \frac{\alpha^2}{\mu} \Delta \Pi = 0, \quad (2)$$

where a prime denotes differentiation with respect to x and

$$\Delta \Pi = -2C(\gamma) \sqrt{\frac{1-x}{x}} \left(-\frac{i\omega}{\alpha} \zeta + \zeta' \right) + \frac{2\omega^2}{\alpha^2} \sqrt{x(1-x)} \zeta. \quad (3)$$

The end-conditions are fixed-free:

$$\zeta(0) = \zeta''(0) = \zeta''(1) = \zeta'''(1) = 0, \quad (4)$$

or clamped-free:

$$\zeta(0) = \zeta'(0) = \zeta''(1) = \zeta'''(1) = 0. \quad (5)$$

1. No inertial fluid loading

Equation (2) reduces to the familiar equation governing small oscillations of an elastic beam when $\Delta \Pi = 0$. This case is important because the associated eigenfunctions can be used to investigate the general fluid loaded and forced motions. When $\Delta \Pi = 0$, the general solution of (2) is¹⁵

$$\begin{aligned} \zeta_n(x) = & a [\cos(k_n x) + \cosh(k_n x)] + b [\cos(k_n x) - \cosh(k_n x)] + \\ & c [\sin(k_n x) + \sinh(k_n x)] + d [\sin(k_n x) - \sinh(k_n x)] \end{aligned} \quad (6)$$

where a, b, c, d and k_n are constants determined by the boundary conditions. For fixed-free conditions we find from (4) that $a = b = 0$ and

$$\zeta_n(x) = \sin(k_n x) + \frac{\sin(k_n)}{\sinh(k_n)} \sinh(k_n x) \quad (7)$$

with k_n determined by the eigenvalue equation

$$\tan(k_n) - \tanh(k_n) = 0. \quad (8)$$

For clamped-free conditions, the application of (5) yields $a = c = 0$ and

$$\zeta_n(x) = [\sin(k_n x) - \sinh(k_n x)] - \frac{\sin(k_n) + \sinh(k_n)}{\cos(k_n) + \cosh(k_n)} [\cos(k_n x) - \cosh(k_n x)] \quad (9)$$

with k_n satisfying

$$\cos(k_n) \cosh(k_n) + 1 = 0. \quad (10)$$

The amplitude of the motion described by either (7) or (9) is arbitrary.

It follows that the general unforced motion of the flag in the absence of unsteady fluid loading consists of a linear superposition of standing waves of the form

$$\xi_n = \zeta_n(x) \exp[-i\omega_n t], \quad \omega_n = k_n^2 \quad (11)$$

where ζ_n, k_n are determined by either (7-8) or (9-10).

2. Influence of inertial fluid loading

Consider a time harmonic solution of the type (1) and expand the amplitude $\zeta(x)$ in terms of the eigenfunctions ζ_n

$$\zeta(x) = \sum_{n=1}^{\infty} a_n \zeta_n. \quad (12)$$

This automatically satisfies conditions (4) or (5). Substitute (12) and (3) into (2) to obtain

$$\begin{aligned} \sum_{n=1}^{\infty} a_n (-\omega^2 + k_n^4) \zeta_n + 2 \frac{\alpha^2}{\mu} C(\gamma) \sqrt{\frac{1-x}{x}} \sum_{n=1}^{\infty} a_n \zeta_n' - \\ 2 \frac{i\omega\alpha}{\mu} C(\gamma) \sqrt{\frac{1-x}{x}} \sum_{n=1}^{\infty} a_n \zeta_n - 2 \frac{\omega^2}{\mu} \sqrt{x(1-x)} \sum_{n=1}^{\infty} a_n \zeta_n = 0. \end{aligned} \quad (13)$$

The coefficients a_n satisfy the infinite system of linear equations obtained by multiplying (13) by $\zeta_m(x)$, integrating over the flag ($0 < x < 1$) and invoking the orthogonality relation (after writing ζ_n in orthonormal form)

$$\int_0^1 \zeta_n \zeta_m dx = \delta_{mn}, \quad (14)$$

where δ_{mn} is the Kronecker delta. This yields

$$\begin{aligned} a_m (-\omega^2 + k_m^4) + 2 \frac{\alpha^2}{\mu} C(\gamma) \sum_{n=1}^{\infty} a_n I_{mn} - \\ 2 \frac{i\omega\alpha}{\mu} C(\gamma) \sum_{n=1}^{\infty} a_n \Phi_{mn} - 2 \frac{\omega^2}{\mu} \sum_{n=1}^{\infty} a_n \Psi_{mn} = 0 \end{aligned} \quad (15)$$

for $m = 1, 2, \dots$, where

$$I_{mn} = \int_0^1 \zeta_m(x) \zeta_n'(x) \sqrt{\frac{1-x}{x}} dx, \quad (16)$$

$$\Phi_{mn} = \int_0^1 \zeta_m(x) \zeta_n(x) \sqrt{\frac{1-x}{x}} dx, \quad (17)$$

$$\Psi_{mn} = \int_0^1 \zeta_m(x) \zeta_n(x) \sqrt{x(1-x)} dx. \quad (18)$$

In accordance with (1) we assume exponential space and time dependence of the free vortex sheet, and write

$$\gamma(x_v, t) = C_0(\omega/\alpha) \exp \left[-i\omega t + i \frac{\omega}{2\alpha} x_v \right]. \quad (19)$$

From (9) we then have

$$C(\omega/\alpha) = \frac{\int_1^{\infty} \frac{x_v}{\sqrt{x_v^2-1}} \exp[-i\omega x_v/2\alpha] dx_v}{\int_1^{\infty} \frac{x_v+1}{\sqrt{x_v-1}} \exp[-i\omega x_v/2\alpha] dx_v}. \quad (20)$$

The eigenfrequencies of self-excited motion are now calculated numerically by truncation of the eigenfunction expansion (12) and the homogeneous system (15) at a suitably large value of $n = N$, leading to a dispersion relation of the form $\omega = \omega(k_1, \dots, k_N, \mu, \alpha)$ and formulae for the ratios of the coefficients a_1, \dots, a_N . Writing $\omega = \omega_r + i\omega_i$, in terms of its real and imaginary parts, we seek to describe the locus of the neutral surface,

$$\omega_i(k_1, \dots, k_N, \mu, \alpha, \omega_r) = 0, \quad (21)$$

across which instability sets in. For clarity of presentation, in much of the following ω_r is replaced by the reduced frequency $\Omega_r = \omega_r/\alpha$, which is equivalent to normalizing the dimensional frequency by the inertial scale U/L rather than U_b/L . We also note that when substituting $\omega_i = 0$, (20) becomes¹²

$$C(\Omega_r) = \frac{H_1^{(2)}(\Omega_r/2)}{H_1^{(2)}(\Omega_r/2) + iH_0^{(2)}(\Omega_r/2)}, \quad (22)$$

and that C_0 in (19), calculated by means of (6), is

$$C_0(\Omega_r) = 4 \frac{i\Omega_r \zeta(1) - \zeta'(1)}{H_1^{(1)}(\Omega_r/2) - iH_0^{(1)}(\Omega_r/2)}, \quad (23)$$

where $H_i^{(j)}$ are Hankel functions of the j th kind and i th order.

B. Numerical results

Note that in calculating the neutral surface (21) the eigenvalues k_n for both fixed-free ($\approx 3.93, 7.07, 10.21 \dots$, see (8)) and clamped-free ($\approx 1.86, 4.69, 7.85 \dots$, see (10)) conditions are invariant, and therefore only the non-dimensional flag mass μ and relative wind velocity α can be prescribed. Our results indicate that excellent convergence of the numerical scheme is achieved when the series (12) is truncated at $N \sim 20$ for all chosen combinations of (μ, α) .

In the following we examine both the quasi-steady aerodynamic approximation¹⁶ and the full solution of the eigenvalue problem. The former considers the limit of a heavy flag ($\mu \gg 1$) in a stiff wind ($\alpha \gg 1$), such that $\beta = \alpha/\sqrt{\mu}$ is finite. Physically, this approximation neglects all unsteady terms in expression (10) for the pressure jump, including the added mass contribution. This greatly simplifies the computations because $C(\gamma) = 1$ (see (20)), and therefore (15) yields

$$a_m (-\omega^2 + k_m^4) + 2\beta^2 \sum_{n=1}^{\infty} a_n I_{mn} = 0. \quad (24)$$

The quasi-steady problem is accordingly governed by the single parameter β and can be formulated as a linear eigenvalue problem for ω^2 .

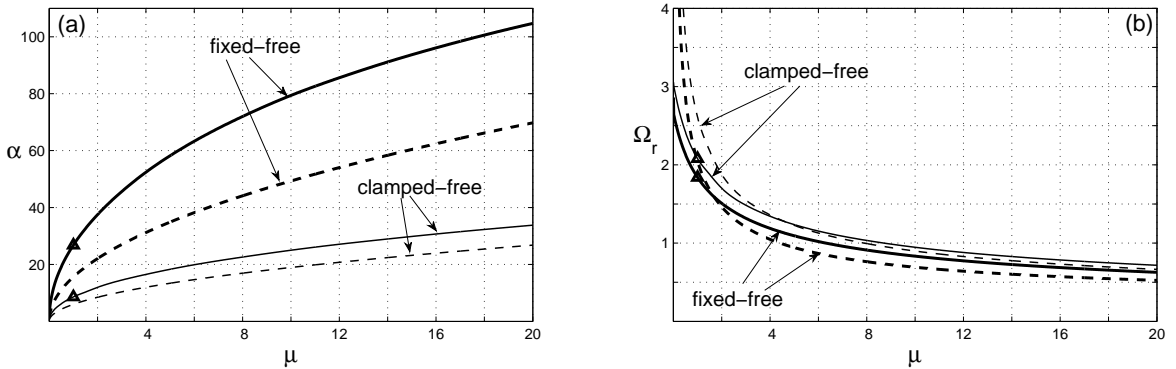


Figure 2. The neutral surface in the (a) (μ, α) plane and the (b) (μ, Ω_r) plane for the quasi-steady (dashed) approximation and full (solid) problem. The bold and thin curves correspond respectively to the fixed-free and clamped-free conditions. The triangles indicate points later referred to in Fig. 4.

Figure 2 illustrate the neutral surface (21) in (a) the (μ, α) plane and (b) the (μ, Ω_r) plane. The solid lines correspond to the full solution and the dashed curves denote the quasi-steady approximation. The thick and thin curves in each part of the figure correspond respectively to the application of the fixed-free and clamped-free boundary conditions. For each value of μ there exists a critical value of the normalized wind speed $\alpha = U/U_b = \alpha_c$ above which instability sets in. For all cases presented, the value of α_c increases monotonically with μ , leading to the intuitive result that heavier flags require a stronger wind to flap. The critical reduced frequency Ω_{r_c} at which instability is excited can be found from the corresponding point in Fig. 2b. In both the quasi-steady (dashed lines) and the full (solid lines) solutions this frequency decreases with μ , indicating that heavier flags start flapping at lower frequencies.

A remarkable result evident from Fig. 2a is the significant stabilizing effect of the fixed boundary condition at the flag pole over the clamped case. Replacing the constraint of a vanishing angle of deflection at the pole with one of zero curvature introduces natural modes of higher frequency ($\omega_n = \sqrt{k_n}$) and therefore more

difficult to excite. Consequently, the value of α_c in the fixed-free case exceeds by the factor of three the clamped-free value at a given μ along most of the curve in the full solution and slightly less than that in the quasi-steady approximation. The differences in the critical reduced frequency are less substantial, although consistently higher values of Ω_{r_c} are observed for the clamped flag.

The quasisteady approximation yields lower critical α_c values in both the fixed-free and the clamped-free cases. This is a consequence of the limit process that neglects the stabilizing effect of added-mass. Yet, this approximation supplies a qualitative picture of the full solution. Our numerical calculation yields for the critical quasi-steady contours in Fig. 2a the approximate formulae $\alpha_c \approx 15.6\sqrt{\mu}$ ($\beta_c \approx 15.6$) and $\alpha_c \approx 5.99\sqrt{\mu}$ ($\beta_c \approx 5.99$) corresponding respectively to the fixed-free and clamped-free cases. The latter differs considerably from the corresponding result obtained by Argentina and Mahadevan,¹¹ who found $\alpha_c \approx 10.53\sqrt{\mu}$ using a different numerical approach. The quasi-steady model is expected to agree quantitatively with the full solution when $\mu, \alpha \gg 1$ and $\Omega_r \ll 1$. As can be seen from Fig. 2b, the latter condition is not satisfied at the presented range of α , yielding the large discrepancies observed in Fig. 2a even for relatively large μ and α . It is only for considerably heavier flags that the quasi-steady approximation becomes a valid quantitative model.

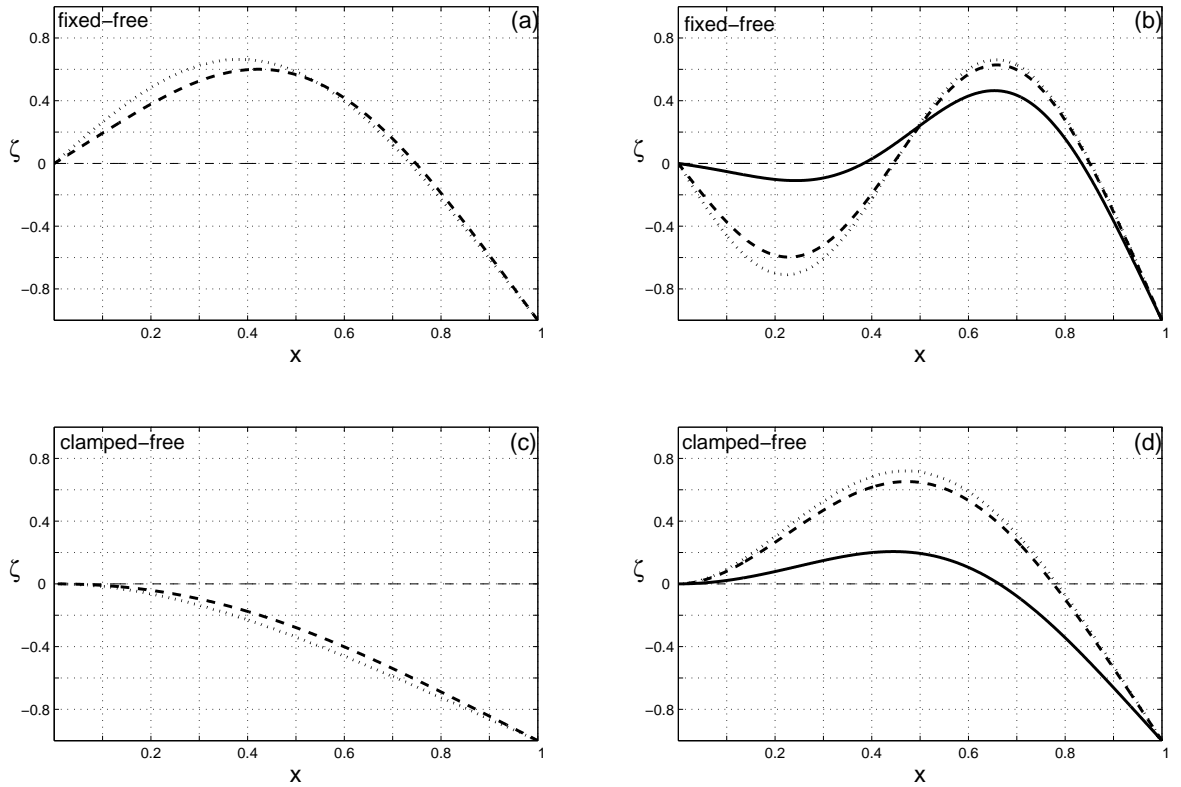


Figure 3. The (a,c) first and (b,d) second modes of motion for the (a,b) fixed-free and (c,d) clamped-free conditions in the absence (dotted lines) and quasisteady approximation (dashed and solid curves) of inertial fluid loading. The dashed lines correspond to neutrally stable modes ($\beta = 5$, $\omega = (18.6, 51.2)$ in (a,b); $\beta = 2$, $\omega = (6.3, 22.5)$ in (c,d)) and the solid lines describe the unstable waves occurring at the onset of instability ($\beta = 15.6$, $\omega = 54.9$ in (b); $\beta = 5.99$, $\omega = 22.5$ in (d)). In the absence of fluid inertia, the frequencies corresponding to the low-order modes (dotted lines) are (15.4, 50.0) in (a,b) and (3.45, 22.0) in (c,d), respectively.

To gain further insight into the mechanism of transition to instability, we show in Figure 3 the dependence of the low-order modes on the single parameter β in the quasi-steady approximation. Parts (a,b) of the figure correspond to the fixed-free problem and parts (c,d) are for the clamped-free case. The first and second modes of motion are given in parts (a,c) and (b,d), respectively. The dashed lines correspond to the stable sub-critical modes for some $\beta < \beta_c$, while the solid lines (in parts (b,d)) are the unstable modes for $\beta = \beta_c$ (numerical values are given in the figure caption). The dotted curves in each figure correspond to

the low-order modes in the absence of inertial fluid loading (see (7) and (9)).

Our numerical calculations invariably yield real values for the eigenfrequencies in the sub-critical conditions of the quasi-steady solution. The corresponding modes are real functions for all $\beta < \beta_c$ (dashed curves). At this sub-critical stage, we observe that the eigenfunctions are similar to their respective natural modes in the absence of inertial fluid loading (dotted lines). With increasing $\beta < \beta_c$, the lowest eigenvalues ($\omega_r = 18.6, 6.3$ in the fixed-free and clamped-free cases, respectively) increase while their associated modes (dashed curves in parts (a,c)) change form. At the same time, the higher second eigenvalue varies only slightly. At the critical value $\beta = \beta_c$ the first two eigenvalues collide on the real axis and split, leading to a *resonance* type of instability¹⁷ manifested as a *standing* wave of increasing amplitude. For $\beta > \beta_c$, one of the modes becomes unstable, with a positive imaginary part and a non-vanishing real part. It is worthwhile to note the considerable differences between the modes in the fixed-free and clamped-free cases: although the qualitative mechanism of instability is similar in both cases, the impact of the different boundary conditions is clearly visible.

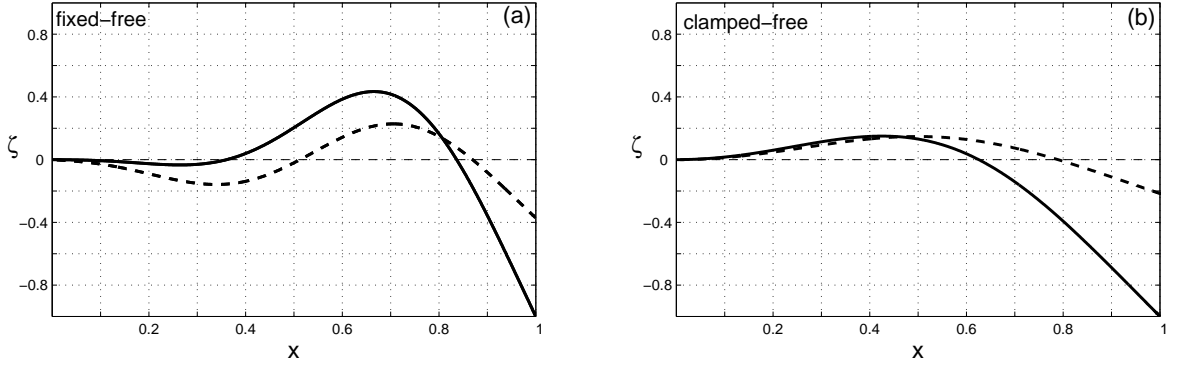


Figure 4. The unstable modes of motion at the onset of instability in the complete problem for the (a) fixed-free ($\mu = 1, \alpha = 26.8, \Omega_r = 1.84$) and (b) clamped-free ($\mu = 1, \alpha = 8.60, \Omega_r = 2.08$) cases. Solid and dashed lines correspond to the real and imaginary parts of $\zeta(x)$, respectively.

The description above may be valid for very heavy flags. The state of affairs changes considerably, however, when $\mu \sim O(1)$, for which it is necessary to solve the complete eigenvalue problem. To illustrate this, Figure 4 presents the unstable modes of motion for the complete problem at the onset of instability for the fixed-free (Fig. 4a) and clamped-free (Fig. 4b) conditions. The critical behaviour is shown for the case $\mu = 1$, indicated by triangles in Fig. 2. Once again, the differences in the mode shapes for the different cases are evident. Unlike in the quasi-steady approximation, the sub-critical behaviour of the flag (i.e., when $\alpha < \alpha_c$ for fixed μ) is stable: all eigenvalues lie in the lower half of the complex plane and the corresponding eigenfunctions contain *both* real and imaginary parts. At $\alpha = \alpha_c$, the lowest eigenmode becomes neutrally stable with $\omega_i = 0$. The solid and dashed lines in the figure correspond to the real and imaginary parts of this mode, respectively, which may also be interpreted as the respective shapes of the flag at $t = 2\pi s/\omega_r$ and $t = (\pi/2 + 2\pi s)/\omega_r$, with $s = 0, 1, 2, \dots$. For $\alpha > \alpha_c$, *flutter* instability occurs, yielding *convecting* waves of increasing amplitude.

IV. The acoustic radiation

In this section we revert to dimensional coordinates for better clarity of presentation. Asterisks, attached to dimensional quantities in Sec. II, are omitted for brevity.

The acoustic pressure is given in the linearized approximation at high Reynolds numbers by¹⁸

$$p_a(\mathbf{x}, t) = p_{a1}(\mathbf{x}, t) + p_{a2}(\mathbf{x}, t) = \rho_0 \frac{\partial}{\partial t} \int_{-\infty}^{\infty} \oint_S v_n(\mathbf{y}, \tau) G_a(\mathbf{x}, \mathbf{y}, t - \tau) dS(\mathbf{y}) d\tau - \rho_0 \int_{-\infty}^{\infty} \int_V (\boldsymbol{\omega} \times \mathbf{U}) \cdot \nabla G_a(\mathbf{x}, \mathbf{y}, t - \tau) d^3\mathbf{y} d\tau, \quad (1)$$

where S is the surface of the flag, $v_n(\mathbf{y}, \tau)$ its normal velocity directed into the fluid and $G_a(\mathbf{x}, \mathbf{y}, t - \tau)$ the acoustic Green's function having vanishing normal derivative on the undisturbed flag. The first integral, $p_{a_1}(\mathbf{x}, t)$, is the pressure contribution due to the flag motion; $p_{a_2}(\mathbf{x}, t)$, given by the second integral, is the pressure produced by the wake. V denotes the fluid region occupied the wake, $\boldsymbol{\omega}$ is the vorticity and \mathbf{U} is the mean stream velocity.

When the frequency of the oscillations is small enough that the flag is acoustically compact, the compact approximation¹⁸

$$G_a(\mathbf{x}, \mathbf{y}, t - \tau) = \frac{1}{4\pi|\mathbf{X} - \mathbf{Y}|} \delta\left(t - \tau - \frac{|\mathbf{X} - \mathbf{Y}|}{c_0}\right) \quad (2)$$

may be applied to evaluate the far-field acoustic radiation. Here $\mathbf{X}(\mathbf{x})$ and $\mathbf{Y}(\mathbf{y})$ denote the *Kirchhoff* vectors for the flag and c_0 is the speed of sound. Substitute (2) into the integral for $p_{a_1}(\mathbf{x}, t)$ and expand to first order in \mathbf{Y} as $|\mathbf{X}| \sim |\mathbf{x}| \rightarrow \infty$, to obtain

$$p_{a_1}(\mathbf{x}, t) \approx \frac{\rho_0}{4\pi|\mathbf{x}|} \frac{\partial}{\partial t} \oint_S v_n\left(\mathbf{y}, t - \frac{|\mathbf{x}|}{c_0}\right) dS(\mathbf{y}) + \frac{\rho_0 x_j}{4\pi c_0 |\mathbf{x}|^2} \cdot \frac{\partial^2}{\partial t^2} \oint_S v_n\left(\mathbf{y}, t - \frac{|\mathbf{x}|}{c_0}\right) Y_j(\mathbf{y}) dS(\mathbf{y}). \quad (3)$$

The first integral, representing a monopole, vanishes because the volume of the flag is constant. The acoustic far-field is therefore of dipole type, determined by the second integral. We approximate $\mathbf{Y}(\mathbf{y})$ by the Kirchhoff vector for a strip of unit width

$$\mathbf{Y}(y_1, y_2) = \left(y_1, \operatorname{Re} \left[-i \sqrt{\left(y_1 - \frac{L}{2} + iy_2 \right)^2 - \frac{L}{4}} \right], y_3 \right), \quad (4)$$

where y_1, y_2, y_3 are the components of the \mathbf{y} -vector in the streamwise $\hat{\mathbf{y}}_1$, flapping $\hat{\mathbf{y}}_2$ and spanwise $\hat{\mathbf{y}}_3$ directions, respectively. Along the flag $y_2 = \pm 0$, $dS = dy_1 dy_3$, $0 \leq y_1 \leq L$ and $0 \leq y_3 \leq l$. In addition,

$$v_n(y_1, t; \omega) = \mp i\omega \exp[-i\omega t] \sum_{n=1}^{\infty} a_n \zeta_n(y_1) \text{ at } y_2 = \pm 0$$

(see (12)). Writing $x_2 = |\mathbf{x}| \cos \theta$ (with $0 \leq \theta \leq \pi$ indicating the observer direction), we find

$$\frac{p_{a_1}(|\mathbf{x}|, \theta, t; \omega)}{\rho_0 U^2} \approx M \frac{l \cos \theta}{2\pi|\mathbf{x}|} \exp\left[-i\omega \left(t - \frac{|\mathbf{x}|}{c_0}\right)\right] F_1(\omega), \quad |\mathbf{x}| \rightarrow \infty \quad (5)$$

where $M = U/c_0$ is the mean stream Mach number and

$$\begin{aligned} F_1(\omega) &= i \left(\frac{\omega}{U} \right)^3 \sum_{n=1}^{\infty} a_n \int_0^L \zeta_n(y_1) \sqrt{y_1(L - y_1)} dy_1 \\ &= i \left(\frac{\omega L}{U} \right)^3 \sum_{n=1}^{\infty} a_n \int_0^1 \frac{\zeta_n(\bar{y}_1)}{L} \sqrt{\bar{y}_1(1 - \bar{y}_1)} d\bar{y}_1. \end{aligned} \quad (6)$$

To calculate $p_{a_2}(\mathbf{x}, t)$, write

$$\boldsymbol{\omega} = \gamma(y_1, t) \delta(y_2) \hat{\mathbf{y}}_3, \quad \mathbf{U} = U \hat{\mathbf{y}}_1, \quad 0 \leq y_3 \leq l \quad (7)$$

to obtain

$$p_{a_2}(\mathbf{x}, t) = -\rho_0 U \int_{-\infty}^{\infty} \oint_S \gamma(y_1, \tau) \frac{\partial G_a}{\partial y_2}(\mathbf{x}, \mathbf{y}, t - \tau) dS d\tau \quad (8)$$

where S denotes the surface of the wake ($y_2 = \pm 0$, $1 \leq y_1 < \infty$ and $0 \leq y_3 \leq l$). Substituting (2) in conjunction with (19) and (4) into (8) and following a procedure similar to the one outlined above for $p_{a_1}(\mathbf{x}, t)$, yields

$$\frac{p_{a_2}(|\mathbf{x}|, \theta, t; \omega)}{\rho_0 U^2} \approx M \frac{l \cos \theta}{2\pi|\mathbf{x}|} \exp\left[-i\omega \left(t - \frac{|\mathbf{x}|}{c_0}\right)\right] F_2(\omega) \quad (9)$$

where

$$\begin{aligned}
F_2(\omega) &= i \frac{\omega C_0(\omega)}{U^2} \int_L^\infty \left(\frac{\partial Y_2}{\partial y_2} \right)_{y_2=0} \exp[i\omega y_1/2U] dy_1 \\
&= i \frac{\omega L}{U} \frac{C_0(\omega)}{U} \int_1^\infty \frac{\bar{y}_1 - 1/2}{\sqrt{\bar{y}_1(\bar{y}_1 - 1)}} \exp[i\omega L \bar{y}_1/2U] d\bar{y}_1 \\
&= -\frac{i\pi}{4} \frac{\omega L}{U} \frac{C_0(\omega)}{U} \exp[i\omega L/4U] H_1^{(1)}(\omega L/4U).
\end{aligned} \tag{10}$$

The total far-field pressure for a compact flag is therefore approximated to first order by the dipole field

$$p_a(|\mathbf{x}|, \theta, t; \omega) \approx M \frac{l \cos \theta}{2\pi |\mathbf{x}|} \exp \left[-i\omega \left(t - \frac{|\mathbf{x}|}{c_0} \right) \right] F(\omega), \quad |\mathbf{x}| \rightarrow \infty, \tag{11}$$

where $F = F_1 + F_2$ is given by the sum of (6) and (10).

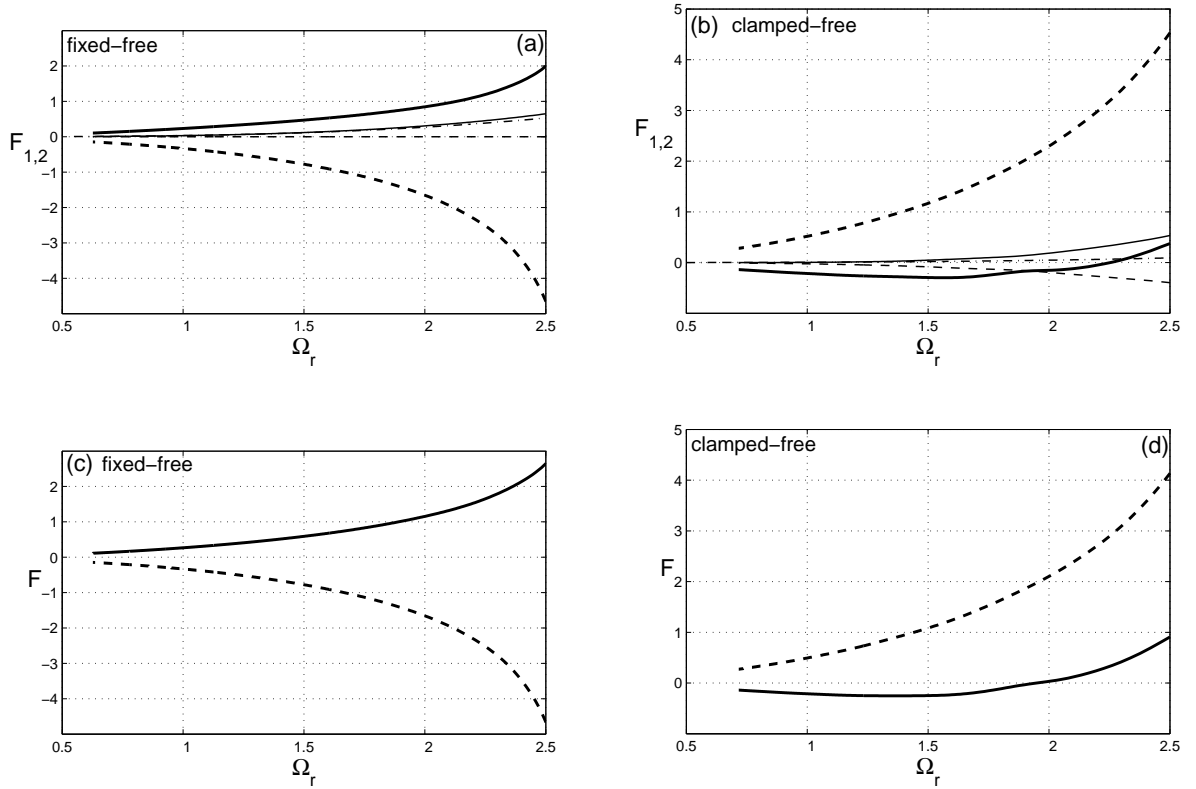


Figure 5. The functions (a,b) F_1 (thick lines), F_2 (thin curves) and (c,d) F at the onset of instability in the (a,c) fixed-free and (b,d) clamped-free cases. The solid and dashed curves correspond to the real and imaginary parts of the functions and the dash-dotted lines describe the quasisteady (real) solution.

The frequency dependence of F_1 , F_2 and F at the onset of instability (where $\omega L/U = \Omega_r$) are illustrated in Figure 5 for the two cases of (a,c) fixed-free and (b,d) clamped-free conditions. The solid and dashed curves correspond to the real and imaginary parts of the functions and the dash-dotted lines show the quasisteady (real) solution. The amplitude of the acoustic pressure increases with the critical reduced frequency Ω_{r_c} . Recalling that Ω_{r_c} itself increases when the flag is lighter (see Fig. 2b), it follows that heavier flags are less noisy than light flags at the onset of motion. There are no significant differences in the overall acoustic amplitudes between the fixed-free and clamped-free cases. However, the wake term, F_2 , is significantly larger than the irrotational flag motion term, F_1 , for all values of Ω_r (Fig 5a,b). Hence, the inclusion of the circulatory pressure jump (8) and the application of the Kutta condition (6) in our model is vital for

the calculation of the far-field radiation. The quasi-steady approximation is close to the complete solution only for small frequencies, where the acoustic radiation becomes negligible and $\alpha \gg 1$. These conditions are indeed in agreement with the above-mentioned limitations of this approximation (see Sec. B), expected to be valid only for very heavy flags.

V. Concluding remarks

We have presented a linear theory for the two-dimensional motion and sound production of an elastic flag in nominally uniform high Reynolds number flow. The analysis permits the calculation of motion and sound production at the very onset of instability, but it cannot determine the resulting final states. Such predictions require consideration of a full non-linear model, of the type suggested in.^{13,14}

Apart from neglecting non-linear effects, the main drawback of our theory is the use made of (3) to describe the irrotational inertial pressure jump across the flag. Essentially, this approximation neglects the curvature ($O(\partial^2 \xi / \partial x^2)$) and time rate of change of the local flag angle ($O(\partial^2 \xi / \partial x \partial t)$), as well as high-order effects. A more general treatment would require the application of a non-local potential, involving integration over the whole flag, and will be studied in a work currently in hand.

The hypothesis (3) follows the simplified model proposed by Theodorsen¹² and applied recently by Argentina and Mahadevan¹¹ to study the onset of motion and sound production for different choices of boundary conditions. The results obtained indicate that a flag that is merely fixed at its pole is considerably more stable than one that is clamped. In the quasi-steady limit of a very heavy flag, instability sets in as a resonance (standing wave of increasing amplitude), while lighter flags exhibit flutter (convective) instability. At the onset of flag motion the dipole-type acoustic far-field of a compact flag is dominated by wake sources. The application of the Kutta condition is therefore of crucial importance in determining the sound. Light flags, characterized by high critical frequencies, are predicted to produce more sound than heavy flags.

References

- ¹PAÏDOUSSIS, M.P. 1998 *Fluid-Structure Interaction: Slender and Axial Flow*. Academic.
- ²HUANG, L. 1995 Flutter of cantilevered plates in axial flow. *J. Fluids Struct.* **9**, 127-147.
- ³WATANABE, Y., SUZUKI, S. SUGIHARA, M. & SUEOKA, Y. 2002b An experimental study of paper flutter. *J. Fluids Struct.* **16**, 529-542.
- ⁴LIAO, J.C., BEAL, D.N., LAUDER, G.V. & TRIANTAFYLLOU, M.S. 2003 Fish exploiting vortices decrease muscle activity. *Science* **302**, 1566-1569.
- ⁵SHEN, L., ZHANG, X., YUE, D.K.P. & TRIANTAFYLLOU, M.S. 2003 Turbulent flow over a flexible wall undergoing a streamwise traveling wave motion. *J. Fluid Mech.* **484**, 197-221.
- ⁶TANEDA, S. 1968 Waving motions of flags. *J. Phys. Soc. Japan* **24**, 392-401.
- ⁷ZHANG, J., CHILDRESS, S., LIBCHABER A. & SHELLEY, M. 2000 Flexible filaments in a flowing soap film as a model for one-dimensional flags in a two-dimensional wind. *Nature* **408**, 835-839.
- ⁸ZHU, L. & PESKIN, C.S. 2002 Simulation of a flapping Flexible filament in a flowing soap film by the immersed boundary method. *J. Comp. Phys.* **179**, 452-468.
- ⁹WATANABE, Y., ISOGAI K., SUZUKI S. & SUGIHARA, M. 2002a A theoretical study of paper flutter. *J. Fluids Struct.* **16**, 543-560.
- ¹⁰SHELLEY, M., VANDENBERGHE, N. & ZHANG, J. 2005 Heavy flags undergo spontaneous oscillations in in flowing water. *Phys. Rev. Lett.* **94**, 094302.
- ¹¹ARGENTINA, M. & MAHADEVAN, L. 2005 Fluid-flow-induced flutter of a flag. *Proc. Natl. Acad. Sci.* **102**, 1829-1834.
- ¹²THEODORSEN, T. 1935 General theory of aerodynamic instability and the mechanism of flutter. NACA Report no. 496.
- ¹³CONNELL, B.H. & YUE, D.K.P. 2007 Flapping dynamics of a flag in a uniform stream. *J. Fluid Mech.* **581**, 33-67.
- ¹⁴ALBEN, S. & SHELLEY, M. 2008 Flapping states of a flag in an inviscid fluid: bistability and the transition to chaos. *Phys. Rev. Lett.* **100**, 074301.
- ¹⁵RAYLEIGH, J.W.S. 1945 *The theory of sound*. Dover.
- ¹⁶BISPLINGHOFF, R.L., ASHLEY, H. & HALFMAN, R.L. 1955 *Aeroelasticity*. Addison-Wesley.
- ¹⁷MARSDEN, J.E. & RATIU, T.S. 1994 *Introduction to Mechanics and Symmetry*. Springer.
- ¹⁸HOWE, M.S. 2003 *Theory of vortex sound*. Cambridge University Press.